Soft Matter

Accepted Manuscript

ROYAL SOCIETY OF CHEMISTRY

www.rsc.org/softmatter

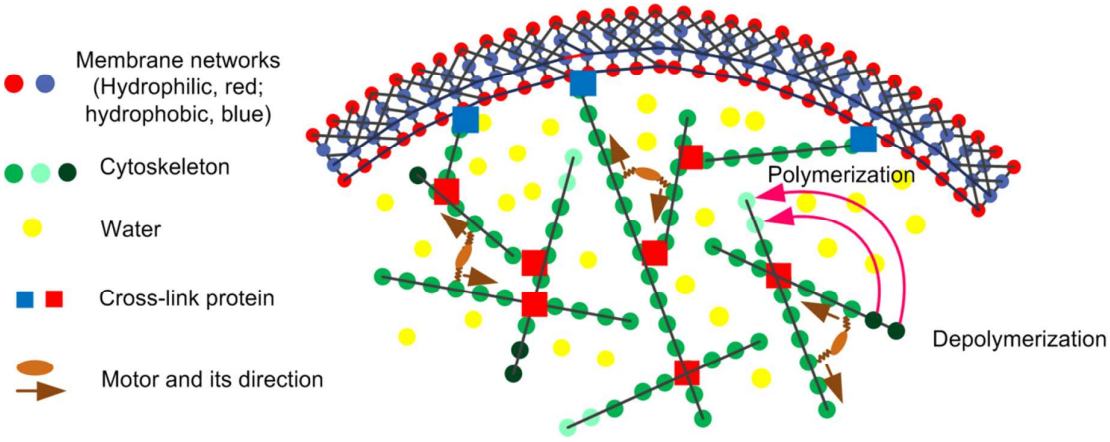

The structure of the cell mechanical model. The cell model contains the membrane networks, the internal cytoskeleton, ACPs, motors and their functions, including the binding/unbinding and the folding/unfolding of the proteins, the polymerization/depolymerization of cytoskeletal filaments, and the walk of motors.

Analyses of the cell mechanical damage in microinjection

Fei LIU[1,2*], Dan WU[3], Xiaoyong WU[1] , Ken CHEN[3]

1. State Key Laboratory of Mechanical Transmission, Department of Mechanical Engineering, Chongqing University, Chongqing, China

2. Departments of Biological Engineering, Massachusetts Institute of Technology, Cambridge, USA

3. Department of Mechanical Engineering, Tsinghua University, Beijing, China

***Corresponding Author**

Fei Liu

Address: Room 315-2, Teaching Building 7,
Chongqing University, Chongqing, 400044,China

Tel:+86-13101328216

E-mail: liufei09@mit.edu

Abstract

The microinjection is an essential technique to introduce foreign materials into biological cells. The soft cell is inevitable ruptured by the microinjector during microinjection. We discuss the way to reduce the mechanical damage by analyzing the control parameters in microinjection. The computational model is developed with the dissipative particle dynamics to simulate the soft mechanical properties of biological cells. The cell model contains the membrane networks, the internal cytoskeleton, crosslink proteins, motors and their functions. The weak power law rheology verifies our computational model. The number of ruptured bonds is used to describe the extent of the mechanical damage that the cell experiences in microinjection. Some experiments are conducted on the zebrafish embryos. Both the simulation works and experiment results show that the size, shapes of the microinjector tip, and the injection velocity have a significant influence on the cell damage. A small, sharp microinjector with a high velocity can reduce the mechanical damage.

Keyworks: microinjection, cell model, dissipative particle dynamics, mechanical damage

1 Introduction of microinjection

With the rapid development of biology, more and more mechanical techniques are used in biological experiments. One of these techniques is the microinjection which is widely used to inject exogenous liquid substances into living cells with a glass microinjector [1, 2]. Single-cell microinjection is utilized in many biological areas[3], such as gene delivery[4, 5], drug development[6], in vitro fertilization[7, 8]. Lots of instruments and robots have been developed to fulfill microinjections. A Semi-automatic microinjection system is introduced by Viigipuu to microinjection of living adherent cells[9]. Sun's group proposed a force control approach to control the penetration force during microinjection[10]. Some commercial system, such as NK2 of Eppendorf Inc. and NT88-V3 of Narishige Inc., are commonly used in lab. These advanced microinjection systems help researchers to control the injection velocity, injection angles and horizontal displacement, etc., which promote the experiments. However, most of these systems above mainly focus on the design of microinjection system, such as the position resolution, the serving control, and the injection force sensing. Little attention has been paid to the harm caused by the microinjection system. During microinjection, the microinjector will penetrate the cell membrane and disorder the organization of the cellular internal structures. This kind of mechanical damage will disturb the normal life of cells; even cause the death of the cells. Thus, we aim to study the mechanical behavior of cells in microinjection and reduce the mechanical damage by optimizing the control parameters of a microinjection system. The control parameters mainly include the size and the tip of the microinjector, the injection angle, the injection velocity, etc. To reduce the mechanical damage, the extent of the damage should be defined at first. However, there is no existing

technique to measure the mechanical damage of a cell. Therefore, one possible way is to build a cell mechanical model and obtain the damage description by the data from the model.

The cell is a complex biological system. It is hard to build an accurate model to describe its mechanical behavior or damage. Some simple mechanical models are already applied to study the cell's behavior in microinjection. Tan and sun used a 'cortical shell - liquid core' model with geometrical boundaries to study the response of a cell in microinjection[11]. They solved the quasi-static equilibrium equations and analyzed the deformation of the cell. Fan focused on the dynamic response of micropipettes during intracytoplasmic sperm injection and proposed a phenomenological Maxwell viscoelastic model. A numerical finite element cell model was developed by Chizari to study the material property of a living cell in microinjection[12]. All these method are continuous models which only provide limited information, such as the injection force, the injection distance and the morphology of cells in microinjection. There is no substantial data that can describe the extent of the cell mechanical damage in these continuous models. To get a better understanding of the cell's mechanical behavior and reduce the harm, a more detailed cell model should be proposed. In this paper, we conduct a computational model based on dissipative particle dynamics to simulate the cellular structure of a cell, and analyze the damage that a cell experiences in microinjection quantitatively.

2 Method

A cell is a complex creature which contains millions of biomolecules such as proteins and nucleic acids. It is hard to cover all the items in a computational model[13]. The experimental have shown that the cell mechanics is mainly determined by its

cytoskeleton[14, 15]. Thus, we mainly focus on the properties of cytoskeleton so as to simplify our model.

2.1 Dissipative particle dynamics

Dissipative particle dynamics (DPD) is a coarse grained technique which widely used to simulate the behavior of biological system, such as the lipid bilayer[16], micelle[17], the red blood cell [18], etc. In DPD, all the particles have the same mass m_0 which is set as the unit of mass, and different types of coarse grained particles represent different kinds of molecules[19]. There are three non-bonded forces between two particles: a conservative force, a dissipative force and a random force.

The conservative force between two particles i and j is

$$\mathbf{F}_{ij}^{C} = \begin{cases} a_{ij}(1-r_{ij}/r_0)\hat{\mathbf{r}}_{ij} & r_{ij} \le r_0 \\ 0 & r_{ij} > r_0 \end{cases} \quad (1)$$

where $\hat{\mathbf{r}}_{ij}$ is the unit vector from particle j to i, and r_{ij} is the distance between the centers of particles i and j. r_0 is the cut-off radius[20]. If $r_{ij} > r_0$, all the three non-bonded forces are zero. a_{ij} is the conservative force parameter gives particles a chemical identity. It represents the maximum repulsive force between interactive-pair particles. A larger a_{ij} represents a stronger repulsive force between particle i and j.

The dissipative force is described by

$$\mathbf{F}_{ij}^{D} = \begin{cases} \gamma_{ij}\omega_{ij}^{D}(\hat{\mathbf{r}}_{ij}\cdot\mathbf{v}_{ij})\hat{\mathbf{r}}_{ij} & r_{ij} \le r_0 \\ 0 & r_{ij} > r_0 \end{cases} \quad (2)$$

where γ_{ij} is the amplitude of the dissipative, and $\mathbf{v}_{ij} = \mathbf{v}_i - \mathbf{v}_j$ is the local velocity vector. ω_{ij}^{D} is the weighting function determined by r_{ij}, $\omega_{ij}^{D} = (1-r_{ij}/r_0)^2$ [21].

The random force between particles i and j is

$$\mathbf{F}_{ij}^{R} = \begin{cases} \sigma_{ij}\omega_{ij}^{R}\theta_{ij}\dfrac{1}{\sqrt{\Delta t}}\hat{\mathbf{r}}_{ij} & r_{ij} \le r_0 \\ 0 & r_{ij} > r_0 \end{cases} \quad (3)$$

where σ_{ij} is the amplitude of the random forces, ω_{ij}^{R} is the random weighting function described by $\omega_{ij}^{R} = (1 - r_{ij}/r_0)$ [21]. θ_{ij} is a randomly fluctuating variable that satisfies Gaussian statistics with zero mean and unit variance. Δt is the step time in simulation. The dissipative force and the random force amplitude follow the relation $\sigma_{ij}^2 = 2\gamma_{ij}k_BT$, where k_BT is the thermal energy. $\gamma_{ij} = 4.5\sqrt{k_BTm_0/r_0^2}$ is used in our computational model[22] . The simulation space is $64 \times 64 \times 64 r_0^3$, and periodic boundary conditions are applied to minimise edge effects. The velocity-Verlet algorithm is used in our model[23] with the simulation time-step $\Delta t = 0.04\sqrt{m_0 r_0^2 / k_BT}$. There are 780000 particles in the simulation space (2.97 per cubic of r_0). The general time cost is ~150 h per simulation with a Intel i7-3520M CPU (2.9GHz).

2.2 Microstructure of the cell

The structures determined the cell mechanical properties mainly include the lipid bilayer, the cortex, the internal cytoskeleton and their functions[14]. To simulate such a structure, we conduct the model shown in Fig.1. In our model, the cell is constructed by the membrane networks, internal cytoskeletal filaments, water, actin crosslink proteins (ACPs) and motor proteins. To simplify our model, the lipid bilayer and the cortex are combined as membrane networks which owns the "hydrophilic hydrophobic hydrophilic" feature of the lipid bilayer and the stiffness of the cortex at

the same time. The complex cytoplasm is represented by the water particles instead of many other substances. The internal cytoskeleton is constructed by microfilaments, intermediate filaments, and microtubules, but we simply use the uniform filaments to mimic its mechanical properties. Besides the physical microstructure of a cell, we also simulate the bio-chemical functions in the cell which influence the mechanical behavior of cells, including the binding/unbinding and the folding/unfolding of the proteins, the polymerization/depolymerization of cytoskeletal filaments, and the walk of motors, Fig.2.

2.2.1 Membrane networks

The membrane networks in our modle combines the "hydrophilic hydrophobic hydrophilic" lipid bilayer and the stiff cortex. The membrane molecular chains are repented as HT_2H, which means there are 2 hydrophilic head particles(H) at the two ends, and 2 hydrophobic tail particles(T) in the middle. The values of conservative force parameters among the water particles (W), the head particles (H) and the tails particles (T) are: $a_{HH}=25$, $a_{HT}=50$, $a_{HW}=35$, $a_{TT}=25$, $a_{TW}=75$, $a_{WW}=25$ (the subscripts represent the types of particles, in units of k_BT/r_0^2)[24], indicating a attractive force between head particles and water particles; a repel force between tail particles and water particles. Therefore, this structure can mimic the "hydrophilic-hydrophobic-hydrophilic" lipid bilayer. To introduce the stiffness of the cortex into the membrane networks, we connect the neighbor HT_2H if the distance between any two particles is less than r_0. The interaction between the connected particles are the same with that of cytoskeletal filaments(section 2.2.2) since cortex is

generally believed to be composed by filaments.

2.2.2 Bond force of the cytoskeletal filament

The cytoskeletal filament is constructed by the cytoskeletal particles, Fig.2a. The adjacent particle i and j are connected in a filament. The bond extension force is determined by the Hookean spring

$$\mathbf{F}_{ij}^{s} = k_s(r_{ij} - r_{eq})\hat{\mathbf{r}}_{ij} \tag{4}$$

where k_s is the extension stiffness with the value $128k_BT$ [25]. r_{eq} is the equilibrium bond length with $r_{eq} = 0.5r_0$.

The bending stiffness of a bond is represented by the three-body potential among adjacent particle triples

$$U_{\varphi(i-1,i,i+1)} = k_\varphi(1-\cos(\varphi-\varphi_0)) \tag{5}$$

where $U_{\varphi(i-1,i,i+1)}$ is the three-body potential, and φ is the bond angle defined by the adjacent particle triples $i-1$, i and $i+1$; φ_0 is the equilibrium bond angle , $\varphi_0 = 0$; k_φ is the bending stiffness with $k_\varphi = 10000k_BT$ corresponding to the experimental value[14]. The bond-bending force is

$$\mathbf{F}_{(i-1,i,i+1)}^{\varphi} = -\nabla U_{\varphi(i-1,i,i+1)} \tag{6}$$

The number of the cytoskeletal particles is determined by the concentration of the f-actin protein(34μM in our model) which obtained from experiments [26, 27]. To achieve the concentration, 56118 cytoskeleton particles are used. The radius of the protein which made the cytoskeleton is $R_G \approx 3.5\text{nm}$ [28]. The cytoskeleton particle radius in our model is $r_G^{model} = 0.5r_0$ (Fig.2). The cell size in our model is $r_{cell}^{model} = 25r_0$.

Provided the cell size in physical is R_{cell}, then the number of the G protein that one particle in our model mimics can be calculated

$$N_G = (\frac{R_{cell}}{r_{cell}^{model}} r_G^{model})^3 / {R_G}^3 \quad (7)$$

The concentration that one particle represented in our model is

$$c = \frac{N_G}{N_A V_{cell}} = \frac{(R_{cell} / r_{cell}^{model})^3 \cdot (r_G^{model})^3 / {R_G}^3}{N_A \frac{4}{3}\pi \cdot {R_{cell}}^3 \times 10^3} \approx 6 \times 10^{-10} (\text{mol/ L}) \quad (8)$$

There are N=56118 cytoskeleton particle in total, therefore, the concentration to real system is

$$C_A = N \cdot c = 34 \mu\text{M/L} \quad (9)$$

Therefore, the concentrations of the components are independent from the cell size.

2.2.3 Polymerization/depolymerization

The cytoskeletal filament is not at a constant length, but highly depolymerized and polymerized[29]. In Fig.2b, we set the polymerization of the filament take place at the +end of the filaments, and the depolymerization at -end. When the distance between a free G-actin particle and a +end particle is less than the equilibrium distance ($0.5r_0$), the polymerization takes place. At the same time, the -end particle at another filament (chosen randomly) should be released from the filament. In this way, we ensure the concentration of the free G-actin at a constant concentration $0.7\mu\text{M}$, which is 2% of that of actin proteins[30], and keep the cell at an equilibrium state.

2.2.4 ACPs

The filaments of the cytoskeleton are not independent but connected by actin

cross-link proteins, such as actin, fimbrin, fascin, and filamin[31]. They mediate the assembly of the filaments to meet the mechanical needs of cells. In our model, the ACPs are freely located in the cytoplasm at the initial state. The concentration of ACPs is $0.7\mu M$. If an ACP is around two filaments and the distances from the ACP to the two filaments are both less than r_0, the ACP links the two filaments, Fig.2c. The torque between the ACP and the filaments are determined by Eq.(10)(11)

$$U_{\varphi} = \frac{1}{2} k_{c,ACP} (\beta - \beta_0)^2 \tag{10}$$

$$U_{\theta} = \frac{1}{2} k_{c,ACP} (\theta_{(1,2)} - \theta_{0(1,2)})^2 \tag{11}$$

where $k_{c,ACP}$ is the torsional stiffness, $k_{c,ACP} = k_{\varphi}$, β is the angle between two connected filaments, and θ_1, θ_2 is the angle between the ACPs and the filaments. β_0, $\theta_{0(1)}$, $\theta_{0(2)}$ are their initial values.

The folding/unfolding force of the ACP is determined by Eq.(12)(13).

$$F(x) = \frac{k_B T}{p_{ACP}} \left(\frac{1}{4} (1 - \frac{x}{L_{ACP}})^{-2} - \frac{1}{4} + \frac{x}{L_{ACP}} \right) \tag{12}$$

$$k_{uf} = \begin{cases} k_{uf}^0 \exp(\dfrac{\lambda_{uf} F}{k_f T}) & if\ r_{12} \geq r_0 \\ 0 & if\ r_{12} < r_0 \end{cases} \tag{13}$$

in which the p_{ACP} is the persistent length of the protein $p_{ACP} = 0.33\text{nm}$, $L = 140\text{nm}$ is the largest distance that a protein can be stretched. $\Delta L = 30\text{nm}$ is the folding length of each fold. k_{uf}^0 is the zero-force unfolding rate coefficient. From the experiments, its reference value is $k_{uf}^0 = 3.0 \times 10^{-5} \text{s}^{-1}$. $\lambda_{uf} = 6 \times 10^{-10}\text{m}$ is the mechanical compliance of the bond for unfolding[32]. The force-extension curve presents a saw

shape which is observed in most proteins[33].

The unbinding of the ACPs is in a similar manner with the unfolding, but with different parameter values $\lambda_{ub} = 1.04 \times 10^{-10}\,\mathrm{m}$, $k_{ub}^{0} = 0.115\,\mathrm{s}^{-1}$ [30]. Once any one of the arms is unbinded, the ACP is free. The unbinded ACP can be rebinded if it meets the binding condition.

2.2.5 Motors

Motors are a class of proteins that are able to move along the filaments and convert chemical energy into mechanical work, which is important for the mechanical properties of cells[34]. The motor in our model is generated in a similar way as the ACP. It has the same properties with ACPs, including the concentration ($0.7\mu\mathrm{M}$), the rotation torque, the unbinding/binding and the unfolding/folding functions. To simulate the movement of motors, we define that the motor walks along the filament following the rules (Fig.2d): one cytoskeletal particle can only be occupied by one ACP or one motor; motors walk from the –end to the +end of the filament; motors cannot pass the occupied particles (by ACPs or other Motors); if a motor meets the +end or occupied particles, it stops walking. The motor moves forward at a cytoskeletal particle per 50 time steps, which is corresponding to the physical value at several hundred nanometers per second. [35]

2.3 Rheology results

The simulation result of our cell mechanical model is show in Fig. 3. It contains the membrane networks, the cytoskeleton, ACPs and motors. Some functions such as depolymerization/polymerization and binding/unbinding, folding/unfolding are also concerned. Seen from Fig. 3, the model mostly agrees with the real structure of a cell.

To verify our model, the modules of the model are obtained since its mechanical properties draw our most attention.

The particle tracking micro-rheology is used to measure the mechanical properties of the model[36]. 47 test particles are choosing from the filament particles as micro beads used in particle tracking micro-rheology. We recorded the time and the position of these beads, and calculated their mean square displacement (MSD) by

$$\left\langle \Delta r(\tau_0)^2 \right\rangle = \left\langle \left| r(t+\tau_0) - r(t) \right|^2 \right\rangle \tag{14}$$

where τ_0 is the lag time. It is proved that the mean square displacement and the lag time follow a power law behavior for an viscoelastic object [37]:

$$\left\langle \Delta r(\tau_0)^2 \right\rangle = \tau_0^{\alpha} \tag{15}$$

where α is the diffusive exponent. If $\alpha = 0$, the object is pure elastic; if $\alpha = 1$, it is pure viscous; when $0 < \alpha < 1$, it is viscoelastic .The experiments on cells proved that $\alpha \approx 0.75$ for a biological cell which suggest that the cell is a viscoelastic object[38].

For a viscoelastic object, the module is

$$\left| G^*(\omega) \right| \approx \frac{k_B T}{\pi a \left\langle \Delta r^2 (1/\omega) \right\rangle \Gamma(1+\alpha(\omega))} \tag{16}$$

where a is the radius of the particle, Γ is the gamma function. Thus, the elastic module $G'(\omega)$ and the viscous part $G''(\omega)$ are

$$\begin{aligned} G'(\omega) &= \left| G^*(\omega) \right| \cos(\pi\alpha(\omega)/2) \\ G''(\omega) &= \left| G^*(\omega) \right| \sin(\pi\alpha(\omega)/2) \end{aligned} \tag{17}$$

The simulation shows that the viscous module is larger than the elastic module at high frequency (>1000 Hz), and smaller than elastic module at low frequency, Fig.4. The slope of the log-log plot presents a weak power law of 0.75 (Fig.4)which is

observed in experiments[39]. When the frequency is at several Hz, the modulus is several Pascal, corresponding to the experiment results 3.21 ± 0.75 Pa [40]. The mechanical modules of the simulation model agree well with the experimental data, which verifies our model.

3 Microinjection simulations and experiments

3.1 Description of mechanical damage

During microinjection, the microinjector will disturb the organization of the cell's structures. However, there is no existing technique to measure this kind of mechanical damage. Since both the molecules in a real cell and the particles in our computational model are connected by bonds, the number of rupture bonds is used to describe the mechanical damage of the cell. It includes all the rupture bonds in our model, such as the ACP's unbinding, the rupture of cytoskeleton filaments, and the rupture of motors. The more bonds ruptured the heavier damage a cell undergoes. Unfortunately, it's hard to count the ruptured bonds in experiments. Therefore, we calculated the injection force in our computational model, since it's much easier to obtain the force-distance relationship in experiments. By comparing the force-distance relation between the computational model and the experiments, the accuracy of our model can be verified. Thus, the number of ruptured bonds in the computational model can estimate the extent of the damage of a cell in microinjection.

3.2 Control parameters

The control parameters are the parameters that can be changed in microinjection and they can probably influence the extent of the cell mechanical damage. There are

five control parameters in general: the microinjector radius, the shape of microinjector tip, the injection velocity, the horizontal displacement and the injection angle. Figure 5 presents the cell morphologies when injected by microinjectors with different control parameters. The microinjector radius is the most important parameter that the researcher concerned in experiments, Fig. 5a. In some high-precision experiments, the tip of the microinjector is required to be some certain shape. The angle ψ between the tip inclined plane and the horizontal plane is used describe the shape of the tips, Fig. 5b. The larger ψ is, the sharper the tip is. If $\psi = 0^{\circ}$, it presents a flat microinjector. The injection velocity determines the velocity that a microinjector penetrate a cell, Fig. 5c. It is hard to keep a microinjector strictly perpendicular to the cell or exactly above the center of the cell in experiments. The nonzero horizontal displacement and the injection angle are inevitable. Therefore the injection angle and the horizontal displacement should be discussed to reduce the damage. The horizontal distance is the distance from the center of a cell to the tips of a microinjector (Fig. 5d) and the injection angle is defined as the angle between the microinjector axis and the vertical line (Fig. 5e).

3.3 Experiments

To verify our computational model, some experiments are conducted on Zebrafish embryo cells. Zebrafish embryos often selected in laboratory due to its advantages of short generation interval, transparent and large size[41, 42]. The experimental devices is TransferMan NK2 (Eppendorf Inc., Resolution: 40nm) microinjection system with the resolution at 40nm/step. During injections, cells are placed on an electronic scale JM-B3003 (Jimin Inc. Capacity/accuracy: 3N/10μN)

which measures the injection force during microinjection. Zebrafish (Danio rerio, AB-type), are selected in our experiments. The aquatic environment is set at 28°C ± 1°C with a light/dark cycle of 14 h/10 h. The approximately 7~8 months old male and female Zebrafish are chosen in pairs the day before microinjection. The selected couple is separated in breeding tanks by a divider which will be removed at ~7:00 am next morning for mating. Some technique is applied to ensure the close properties of all the tested cells: 1) All the Zebrafish embryos tested are from the same parents. 2) To avoid the differentiation, the experiments are finished within 1 hour after the Zebrafish embryos were born. Several serial experiments are conduct to analyze the influence of control parameters.

The radius of the Zebrafish embryo is 350 ~ 450μm so we set the radius of the simulated cell in the computational model to be 400μm and adjust the time scale to agree with the velocity we used in experiments. The injection force in the computational model and the experiments verifies the accuracy of our simulation results. Therefore, the number of the ruptured bonds in simulation can describe the damage of the cell. By comparing the numbers of the ruptured bonds with different control parameters, we optimize these parameters and reduce the mechanical damage.

The interactions between the microinjector particles and the other kind of particles generate the injection force F_{inj}^{model} (in unit of 1). We should match them in unit of Newton. Here, we use the rupture force for one filament to bridge the model and the realistic. The radius of the protein is $R_G \approx 3.5\text{nm}$. The cytoskeleton particle radius in our model is $r_G^{model} = 0.5r_0$ (Fig.2). Seen from the cross section of one filament, the number of real filaments that one cytoskeletal filament in the DPD model represented is

$$N_{filament} = (\frac{R_{cell}}{r_{cell}^{model}} r_G^{model})^2 / R_G{}^2 \quad (18)$$

Experimental data shows that the rupture force for one real filament is f_0 ($\approx$110pN from Ref. 43[43]), thus, the real rupture force (in unit of Newton) for one filament in our model is

$$F_0 = N_{filament} \cdot f_0 \quad (19)$$

During simulation, we can obtain the rupture force for one filament is $F_{filament}^{model}$ (in unit of 1), By comparing the rupture force for one filament in realistic and in DPD model, we can obtain the actual injection force is

$$F_{inj} = F_{inj}^{model} \cdot \frac{F_0}{F_{filament}^{model}} \quad (20)$$

4 Results and discussions

4.1 The radius of the microinjector

Four microinjector radii are simulated in our computational model (Fig.5a) and the injection force-distance relation is shown in Fig.6a. Accordantly, four microinjector radii are tested in the experiments. Because large microinjector radius is seldom used in experiment, we choose the radii at $2.5\,\mu m$, $10\,\mu m$, $20\,\mu m$ and $30\,\mu m$. For each radius, 3~4 Zebrafish embryo cells are injected, and the microinjector moves at a constant velocity ($20\,\mu m/s$) for each injection. The injection force is present in Fig. 6b. Both the computational results (Fig.6a) and the experimental results (Fig. 6b, part of the data can be found in our previous publication[44]) suggest that the injection force increases as the microinjector moving towards the cell. The four curves of different microinjector radius are almost overlapped at beginning parts, Fig. 6b. For

example, when the injection distance is ~50μm, the injection forces for all the four radii are ~ 90μN (Fig. 6b). The similar situations are found in computational work, Fig.6a. The consistency between the computational work and the experiments verify our cell model. The numbers of ruptured bonds during microinjection are shown in Fig. 6c. It illustrates that the extent of damage increases as the microinjector penetrates the cell. Once the membrane is ruptured, the number of ruptured bonds rises slowly. The four curves in Fig. 6c suggest that the larger microinjector radius causes more ruptured bonds or heavier damage. Therefore, the small microinjector should be used to reduce the mechanical damage in experiment.

4.2 The shape of the microinjector tips.

To analyze the influence of microinjector tips, three microinjetor with different tip shapes ($\psi = 30^{\circ}, 45^{\circ}$ and 60°) are simulated in computational model (Fig.5b) and tested in experiments (Fig.7). The injection force-distance relations are shown in Fig.8a (simulation) and Fig. 8b (experiment). They suggest that a sharp tip generates small injection force and penetrate the cell membrane more easily. The numbers of rupture bonds presented in Fig. 8c indicate that the sharper tip leads to the smaller extent of the damage to cells.

4.3 The injection velocity

Different velocities, $v = 5\mu$m/s, $v = 20\mu$m/s and $v = 50\mu$m/s, are applied in the computation model and experiments. The two results agree with each other (Fig.9a, b). The larger velocity causes the larger injection force, and requires a larger injection distance to rupture the membrane. However, the smaller velocity generates more

number of ruptured bonds (Fig. 9c), which indicates that we should penetrate quickly in microinjection to reduce the damage.

4.4 The horizontal displacement and the injection angle

Three groups of control parameters, $x = 200\mu m$, $\theta=0^{\circ}$; $x = 0\mu m$, $\theta=0^{\circ}$ and $x=0\mu m$, $\theta=10^{\circ}$ are tested to analyze the effects of the horizontal displacement(Fig. 5d) and the injection angle(Fig.5e). There are no significant differences for the three groups, neither in the injection force (Fig.10ab) or the number of ruptured bonds (Fig.10c), which suggests that both the injection angle and the horizontal distance have a little influence on the cell mechanical damage. However, it does not mean that we can use any injection angle or horizontal distance. The experience in experiments tells us that the large injection angle or horizontal distance can break the microinjetor which owns a large radius- length ratio and very fragile to the horizontal force. We should avoid the large injection angle and the injection horizontal distance.

Based on our simulation and experimental results, the microinjector radius (corresponding to the membrane openings) and the velocity (corresponding to the time) are the most important factors for the cell's survival rate.

5 Conclusion

More and more mechanical techniques are used in bioengineering. The mechanical damage to the bio-system caused by these techniques should be concerned. We take the microinjection as an example to study the mechanical behavior of the cell and reduce the damage by optimizing the control parameters. Firstly, we developed a computational cell model with the dissipative particle dynamics simulation. The membrane networks, the internal cytoskeleton, the ACPs, motors and their functions

are simulated in our model. The simulation results show that the cell is a viscoelastic object with a weak power law. Then, we simulated the processes that the microinjector penetrates the cell with different control parameters and some experiments on the zebrafish embryos are conducted. The number of ruptured bonds is used to describe the damage of the cell in microinjection. Both the computational and experimental results show that the small radius of the microinjector, the sharp microinjector tips, and the large injection velocity can reduce the damage of the cell.

Acknowledgements

The authors would like to thank Prof. Roger D. Kamm at Massachusetts Institute of Technology for his insightful suggestions and also gratefully acknowledge the financial support for portions of this research from the Fundamental Research Funds for the Central Universities under Grant No. CDJZR14905502, the National Natural Science Foundation of China under Grant No. 51175278, and the Singapore-MIT Alliance for Research and Technology.

The authors declare no conflict of interest.

References

1. L. Tesson, C. Usal, S. Ménoret, E. Leung, B. J. Niles, S. Remy, Y. Santiago, A. I. Vincent, X. Meng and L. Zhang, *Nat Biotechnol*, 2011, **29**, 695-696.
2. B. Wefers, M. Meyer, O. Ortiz, M. H. de Angelis, J. Hansen, W. Wurst and R. Kühn, *Proceedings of the National Academy of Sciences*, 2013, **110**, 3782-3787.
3. Y. Zhang and L. C. Yu, *Bioessays*, 2008, **30**, 606-610.

4. A. J. Mellott, M. L. Forrest and M. S. Detamore, *Ann Biomed Eng*, 2013, **41**, 446-468.
5. F. K. Wong, C. Haffner, W. B. Huttner and E. Taverna, *Nature protocols*, 2014, **9**, 1170-1182.
6. L. Zema, G. Loreti, A. Melocchi, A. Maroni and A. Gazzaniga, *J Control Release*, 2012, **159**, 324-331.
7. T. Bongso, A. Sathananthan, P. Wong, S. Ratnam, S. Ng, C. Anandakumar and S. Ganatra, *Hum Reprod*, 1989, **4**, 175-179.
8. Z. Ivics, L. Hiripi, O. I. Hoffmann, L. Mátés, T. Y. Yau, S. Bashir, V. Zidek, V. Landa, A. Geurts and M. Pravenec, *Nature protocols*, 2014, **9**, 794-809.
9. K. Viigipuu and P. Kallio, *ATLA (Alternatives To Laboratory Animals) Journal*, 2004, **32**, 417-423.
10. Y. Xie, D. Sun, C. Liu, H. Tse and S. H. Cheng, *The International Journal of Robotics Research*, 2010, **29**, 1222-1232.
11. Y. Tan, D. Sun, W. Huang and S. H. Cheng, *NanoBioscience, IEEE Transactions on*, 2010, **9**, 171-180.
12. J. F. Diaz, N. Olgac, M. Karzar-Jeddi and T.-H. Fan, *Journal of Medical Devices*, 2010, **4**, 024502.
13. D. Stamenović and D. E. Ingber, *Biomechanics and modeling in mechanobiology*, 2002, **1**, 95-108.
14. J. Stricker, T. Falzone and M. L. Gardel, *J Biomech*, 2010, **43**, 9-14.
15. D. A. Fletcher and R. D. Mullins, *Nature*, 2010, **463**, 485-492.
16. A. Sevink and J. Fraaije, *Soft Matter*, 2014, **10**, 5129-5146..
17. M.-T. Lee, A. Vishnyakov and A. V. Neimark, *The Journal of Physical Chemistry B*, 2013, **117**, 10304-10310.

18. Z. Peng, X. Li, I. V. Pivkin, M. Dao, G. E. Karniadakis and S. Suresh, *Proceedings of the National Academy of Sciences*, 2013, **110**, 13356-13361.
19. P. Espanol, in *Handbook of Materials Modeling*, Springer, 2005, pp. 2503-2512.
20. G. Illya, R. Lipowsky and J. Shillcock, *J. Chem. Phys.*, 2005, **122**, 244901.
21. P. Espanol and P. Warren, *EPL (Europhysics Letters)*, 1995, **30**, 191.
22. V. Ortiz, S. O. Nielsen, D. E. Discher, M. L. Klein, R. Lipowsky and J. Shillcock, *The Journal of Physical Chemistry B*, 2005, **109**, 17708-17714.
23. R. D. Groot and P. B. Warren, *J Chem Phys*, 1997, **107**, 4423.
24. J. C. Shillcock and R. Lipowsky, *The Journal of chemical physics*, 2002, **117**, 5048-5061.
25. L. Gao, J. Shillcock and R. Lipowsky, *J. Chem. Phys.*, 2007, **126**, 015101.
26. H. Lodish, A. Berk, S. L. Zipursky, P. Matsudaira, D. Baltimore and J. Darnell, Molecular Cell Biology (4th ed), W. H. Freeman, 2000.
27. T. Kim, Massachusetts Institute of Technology, master's thesis (advisor: Roger D. Kamm) 2007.
28. T. Kim, W. Hwang and R. Kamm, *Exp Mech*, 2009, **49**, 91-104.
29. D. M. Wetzel, S. Håkansson, K. Hu, D. Roos and L. D. Sibley, *Mol Biol Cell*, 2003, **14**, 396-406.
30. T. Kim, Massachusetts Institute of Technology, doctoral dissertation (advisor: Roger D. Kamm) , 2011.
31. N. Kureishy, V. Sapountzi, S. Prag, N. Anilkumar and J. C. Adams, *Bioessays*, 2002, **24**, 350-361.
32. J. M. Ferrer, H. Lee, J. Chen, B. Pelz, F. Nakamura, R. D. Kamm and M. J. Lang, *Proceedings of the National Academy of Sciences*, 2008, **105**, 9221-9226.
33. M. Carrion-Vazquez, A. F. Oberhauser, S. B. Fowler, P. E. Marszalek, S. E.

Broedel, J. Clarke and J. M. Fernandez, *Proceedings of the National Academy of Sciences*, 1999, **96**, 3694-3699.

34. J. Howard, Mechanics of Motor Proteins and the Cytoskeleton, Sinauer associates. 2001.
35. P. Pierobon, S. Achouri, S. Courty, A. R. Dunn, J. A. Spudich, M. Dahan and G. Cappello, *Biophys J*, 2009, **96**, 4268-4275.
36. S. Yamada, D. Wirtz and S. C. Kuo, *Biophys J*, 2000, **78**, 1736-1747.
37. T. Mason, K. Ganesan, J. Van Zanten, D. Wirtz and S. Kuo, *Phys Rev Lett*, 1997, **79**, 3282.
38. J. C. Crocker and B. D. Hoffman, *Methods Cell Biol.*, 2007, **83**, 141-178.
39. L. Deng, X. Trepat, J. P. Butler, E. Millet, K. G. Morgan, D. A. Weitz and J. J. Fredberg, *Nature materials*, 2006, **5**, 636-640.
40. E.-M. Schötz, R. Burdine, M. Steinberg, C.-P. Heisenberg, R. Foty and F. Julicher, Dynamics and Mechanics of Zebrafish Embryonic Tissues, VDM Verlag, 2008.
41. A. Nasevicius and S. C. Ekker, *Nat. Genet.*, 2000, **26**, 216-220.
42. W. Wang, X. Liu, D. Gelinas, B. Ciruna and Y. Sun, *PLoS ONE*, 2007, **2**, e862.
43. A. Kishino and T. Yanagida, Nature, 1988, **334**, 74-76.
44. F. Liu, D. Wu and K. Chen, *Journal of the mechanical behavior of biomedical materials*, 2013, **24**, 1-8.

Figure legends

Figure 1

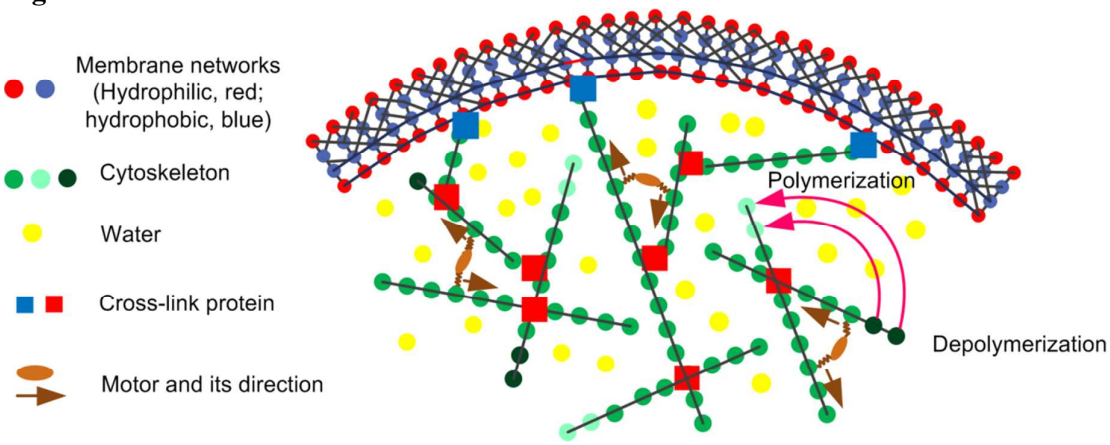

Figure 1 The structure of the cell mechanical model. The cell model contains the membrane networks, the internal cytoskeleton, ACPs, motors and their functions, including the binding/unbinding and the folding/unfolding of the proteins, the polymerization/depolymerization of cytoskeletal filaments, and the walk of motors.

Figure 2

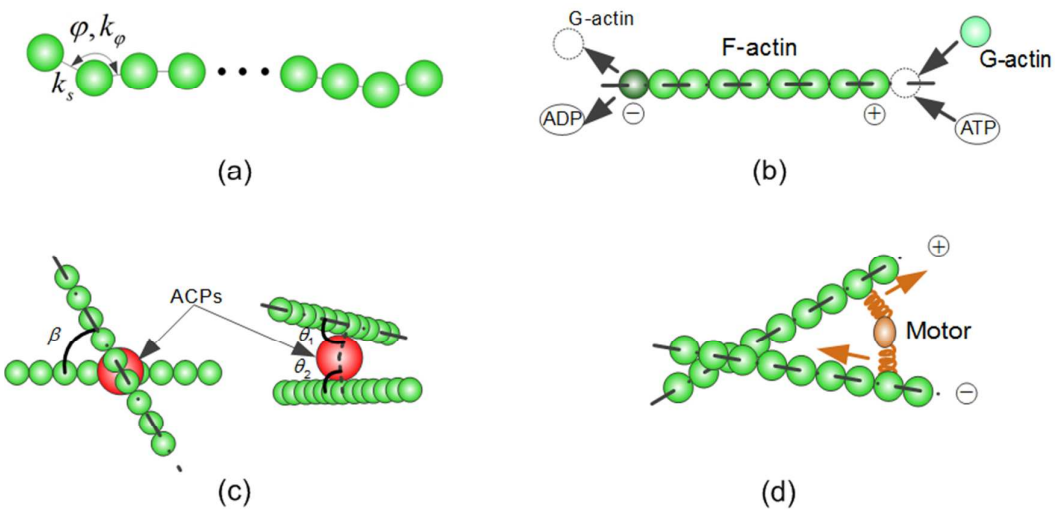

Figure 2 The features of the cell model. (a) the filament owns bending and extension stiffness; (b) The polymerization and depolymerization of filaments; (c) The ACP and its connected filaments; (d) The walk of the motor in the model.

Figure 3

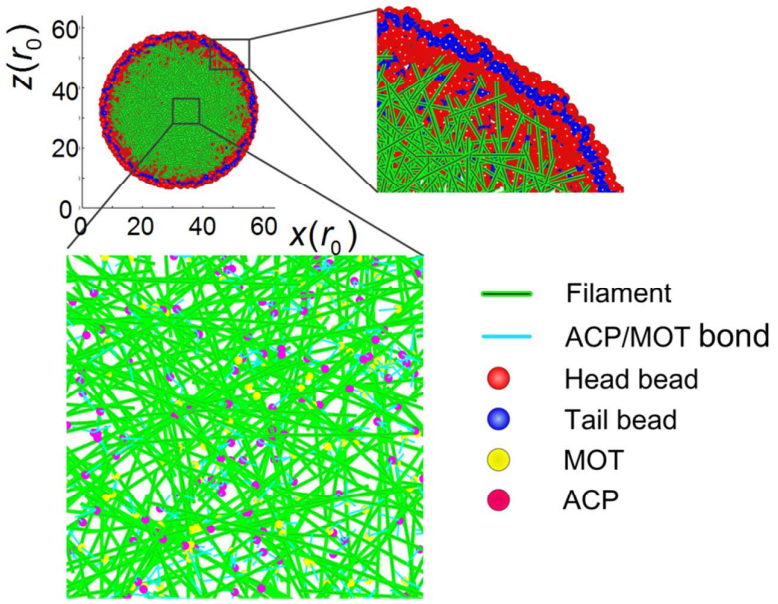

Figure 3 The computational cell mechanical model.

1 **Figure 4**

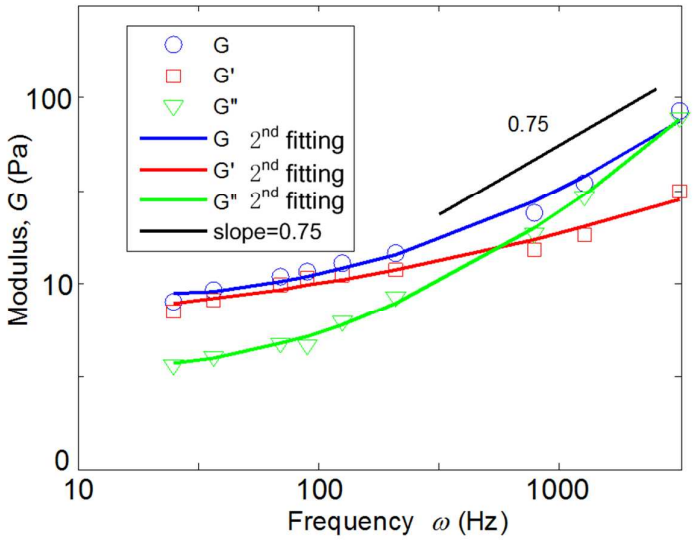

2

3

4 **Figure 4** The modulus of the cell model. The 2nd fitting lines present the curve fitting

5 with the second degree polynomial. The viscous module is larger than the elastic

6 module at high frequency but smaller than elastic module at low frequency. The slope

7 of the log-log plot is ~0.75.

8

Figure 5

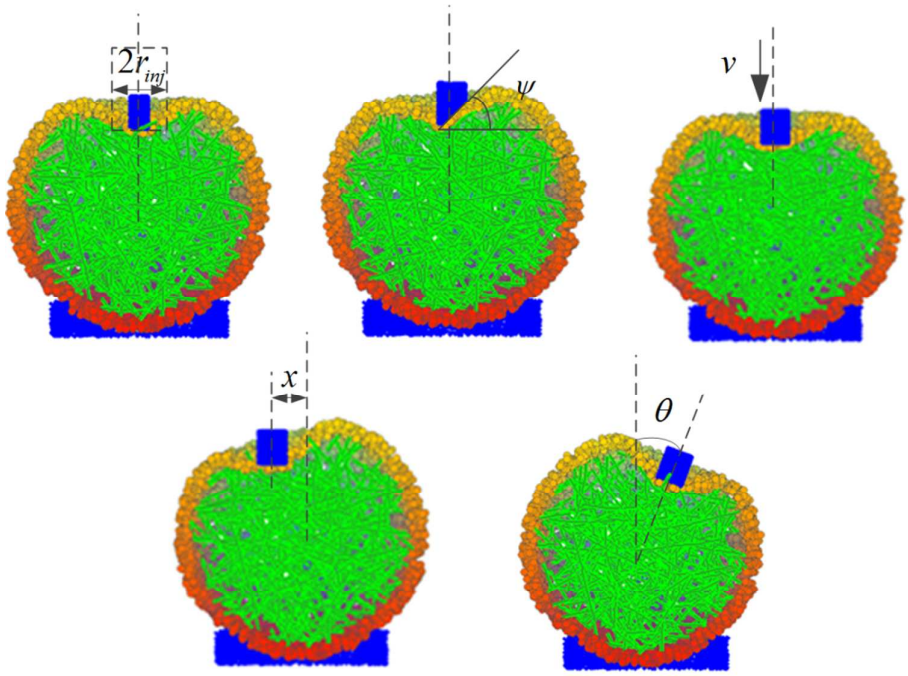

Figure 5 The control parameters which influence the microinjection. (a) the microinjector radius;(b) the shape of the microinjector tip; (c) the injection velocity; (d) the horizontal displacement; (e)the injection angle.

1 **Figure6**

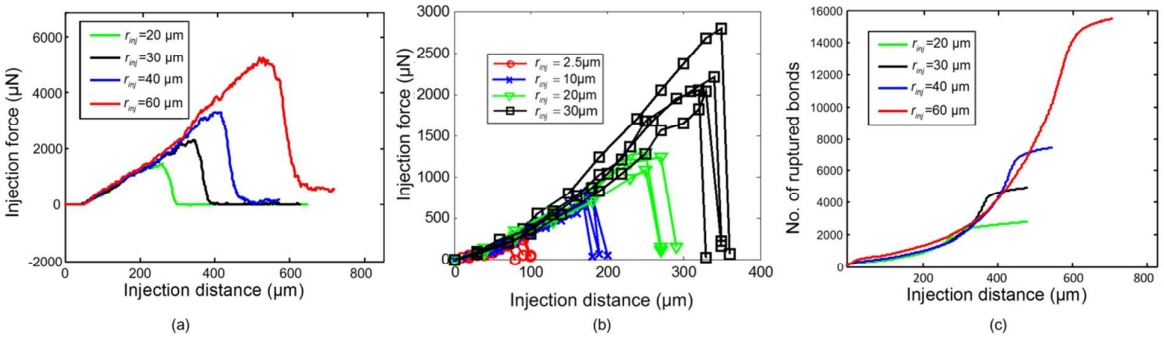

2

3 **Figure 6** Results of the microinjection with different microinjector radius. (a) the

4 injection force-distance relation(simulation); (b) the injection force-distance

5 relation(experiment[42]); (c) the number of ruptured bonds(simulation).

6

Figure 7

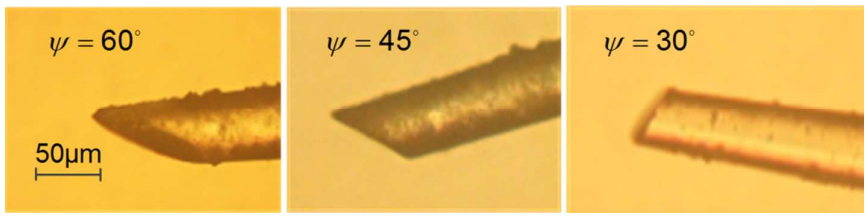

Figure 7 The microview of the shapes of microinjection tips.

Figure 8

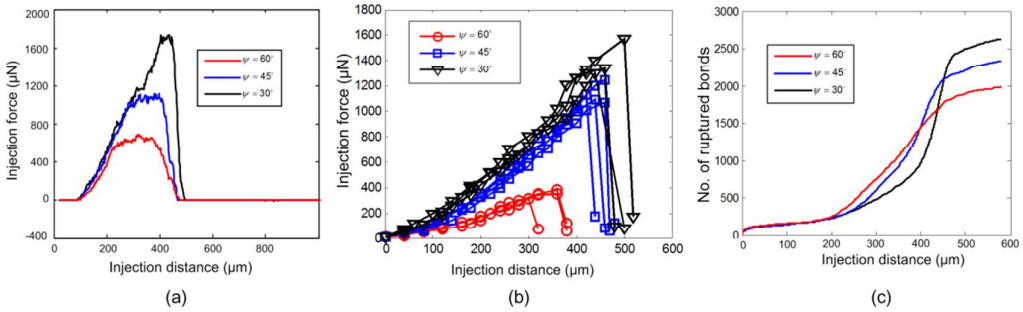

Figure 8 Results of the microinjection with different microinjector tips. (a) the injection force-distance relation (simulation); (b) the injection force-distance relation(experiment); (c) the number of ruptured bonds(simulation)

Figure 9

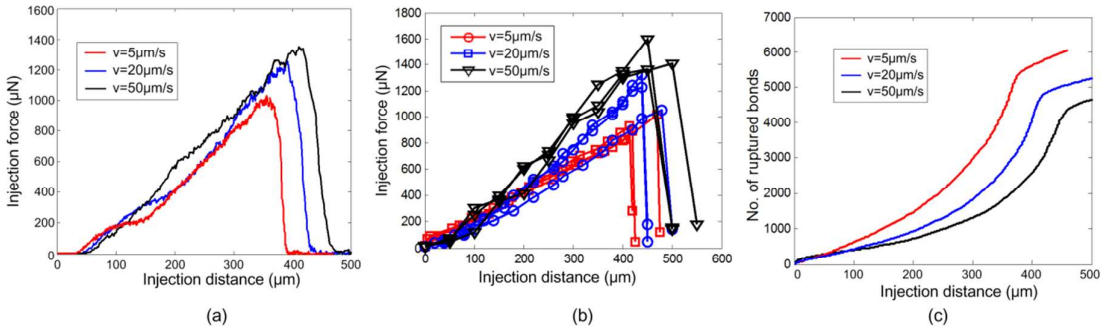

Figure 9 Results of the microinjection with different injection velocities. (a) the injection force-distance relation (simulation); (b) the injection force-distance relation(experiment); (c) the number of ruptured bonds(simulation)

Figure 10

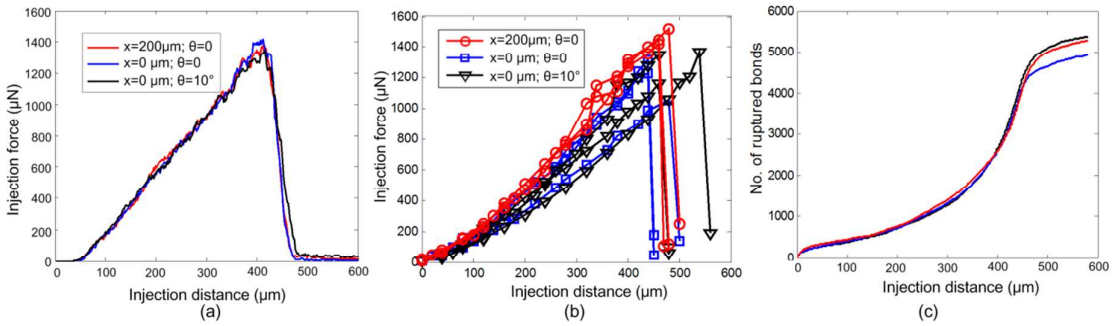

Figure 10 Results of the microinjection with different horizontal displacements and injection angels. (a) the injection force-distance relation (simulation); (b) the injection force-distance relation(experiment); (c) the number of ruptured bonds(simulation)